Highlights

- In civil engineering structural safety often relies on safety coefficients.
- Damage tolerance may help to improve structural safety.
- Damage tolerance is presented for designing prestressing anchorages (PA).
- 2D and 3D FE models are used for assessing damage tolerance of PA.
- A specific anchorage geometry is analysed to show the effectiveness of this approach.

Damage tolerance in engineering components: Implementation to anchor heads

M.A. Olivares[1], J.C. Gálvez[1], F.Suárez[2]

[1]*Universidad Politécnica de Madrid, Departamento de Ingeniería Civil-Construcción, E.T.S.I. de Caminos, Canales y Puertos, C/ Prof. Aranguren s/n, 28040 Madrid, Spain*

[2]*Departamento de Ingeniería Mecánica y Minera. Universidad de Jaén. Campus Científico-Tecnológico de Linares. Cinturón Sur 23700 – Linares (Jaén), Spain*

Abstract

Damage tolerance is commonly used as a design criterion in some engineering fields, such as aerospace engineering, but is not usual in civil engineering, where structural safety often relies on safety coefficients. This work presents a study on how using damage tolerance for designing post-tensioning anchor heads, usual mechanisms in many civil engineering works, can be useful for building safer structures. Damage is simulated using 2D and 3D finite element models, considering axisymmetric damage and single damage. The influence of several aspects, such as the crack depth, the crack orientation angle or the shape of the anchorage, is studied. Finally, a specific anchorage geometry is analysed using the damage tolerance concept to show that this approach may help in the design of this type of elements.

Keywords: Damage tolerance, post-tensioning anchor head, stress intensity factor, Finite Element Method

1. Introduction

The concept of damage tolerance in engineering design is based on the assumption that any structural element can have flaws that can limit their life with usage [1]. Design based on damage tolerance is a common practice in aerospace engineering [2, 3] and nuclear engineering [4, 5], but not so usual in more traditional fields, such as civil engineering, where design is based on considering components without any defect.

Nevertheless, in real practice, structural components do present defects due to the manufacturing process, transport or assembly, for instance. These possible imperfections are usually considered to be covered by safety coefficients used in the design project, which lead to designing elements under magnified loads and considering materials with lower strength properties. This approach provides a simple procedure for computing the strength of structural components but provides no guidance to estimate its life when a crack grows as a consequence of an overload, repeated loads or under an aggressive environment.

As observed by Valiente and Elices [6], the usual design criteria, such as yield strength, ultimate strength and ductility, may not avoid problems leading to brittle fracture. This fact has

attracted the attention of several authors in the last years and interesting contributions focused on the damage tolerance concept applied in the construction field can be found analysing structural details, such as post-tensioning systems [7], bolted joints [8], prestressing steel wires [9], rods [10], composite elements under impact loading [11] or railway axles [12-16], proving that this approach can help with the maintenance program of railway infrastructures.

More specifically, the concept of damage tolerance can be particularly useful to study anchorage systems used in prestressed concrete elements [17] or prestressed systems anchored to rock [18], since these elements, which work under high stress states, are prone to early damage if small defects are present.

In this paper, a simple methodology is described for designing structural elements based on the concept of damage tolerance. A post-tensioning anchorage used in prestressed concrete elements is analysed as a case study to illustrate this methodology. Damage, such as corrosion pits or dents, is idealised as tiny cracks, a hypothesis from the safe side. When brittle fracture occurs – the worst scenario – fracture loads can be computed using linear elastic fracture mechanics. This work provides some clues for: (a) computation of stress intensity factors in involved geometries, such as anchor heads and (b) the measurement of the material fracture toughness under the corresponding working conditions. The paper ends with an example where the damage tolerance of an anchor is evaluated based on values taken from actual failures.

2. Damage simulation

2.1. The damaged component

Steel tendons with end anchorages are used to transfer compressive loads to concrete. The performance of anchorages is a complex problem and, in general, is designed by experience, tests, and usage, rather than by theory [19].

As already mentioned, defects —in the form of corrosion pits, scratches or dents— can appear and act as stress raisers, similar to small cracks. Such cracks, depending on the stress acting on them or on the environment, can grow and become unstable, leading to the eventual anchorage failure.

To apply the concept of damage tolerance, the anchor head has to be modelled with an initial damage and a crack is probably the simplest approach. The safest procedure is to place the crack in the worst place, usually inside the most tensile stressed region of the anchor head. With such approach, two anchor head geometries are evaluated in this research; a circular plate and a simple anchor head.

2.2. A circular plate transversally loaded

A transversally loaded circular plate is an idealized structural component that can be found in practice. The purpose of this section is to evaluate when an initial defect in the form of a crack will start growing. This process is a function of the plate geometry, the crack size and its location.

Two types of cracks were taken into consideration; a simple crack and a circular crack surrounding the whole anchor head. Both of them are located on the tensile face. Consequently, two types of finite element models were used: a two dimensional axisymmetric model for the circular crack and a three dimensional model for the simple crack. The circular crack is considered here because of its simplicity and is used as a simple procedure to find upper or lower bounds of the problem.

2.2.1. Two-dimensional axisymmetric calculation

A disc of radius 1.34R and thickness H is considered and five values of H/R are analysed; H/R = 0.25, 0.50, 0.75, 1.00 and 1.25. A uniform load P is distributed on a circle of radius R. The disc is simply supported and nine different crack sizes are analysed; a/H = 0.001, 0.002, 0.005, 0.01, 0.02, 0.05, 0.1, 0.2 and 0.5, where a stands for the crack depth. Cracks are located on the tensile side of the plate, at distance r from the symmetric axis of the plate. Two different locations were considered, r= R/2 and R/4 (see Figure 1a).

The model was built with the finite element code ANSYS. Quadrilateral elements of eight nodes were used in order to generate the finite element mesh. The mesh at the crack location is refined due to the stress singularity at the crack tip.

As shown in Figure 2, the mesh at the crack tip was generated by means of 12 quarter point 8-node quadrilateral elements forming a rosette on which every element shares one of its nodes at the crack tip location. This allows evaluating the stress intensity factor by means of the fit of the nodal displacements in the vicinity of the crack tip. The size of the first row of elements was set to 1/10 of the crack depth a in order to obtain accurate values of the stress intensity factors (SIF).

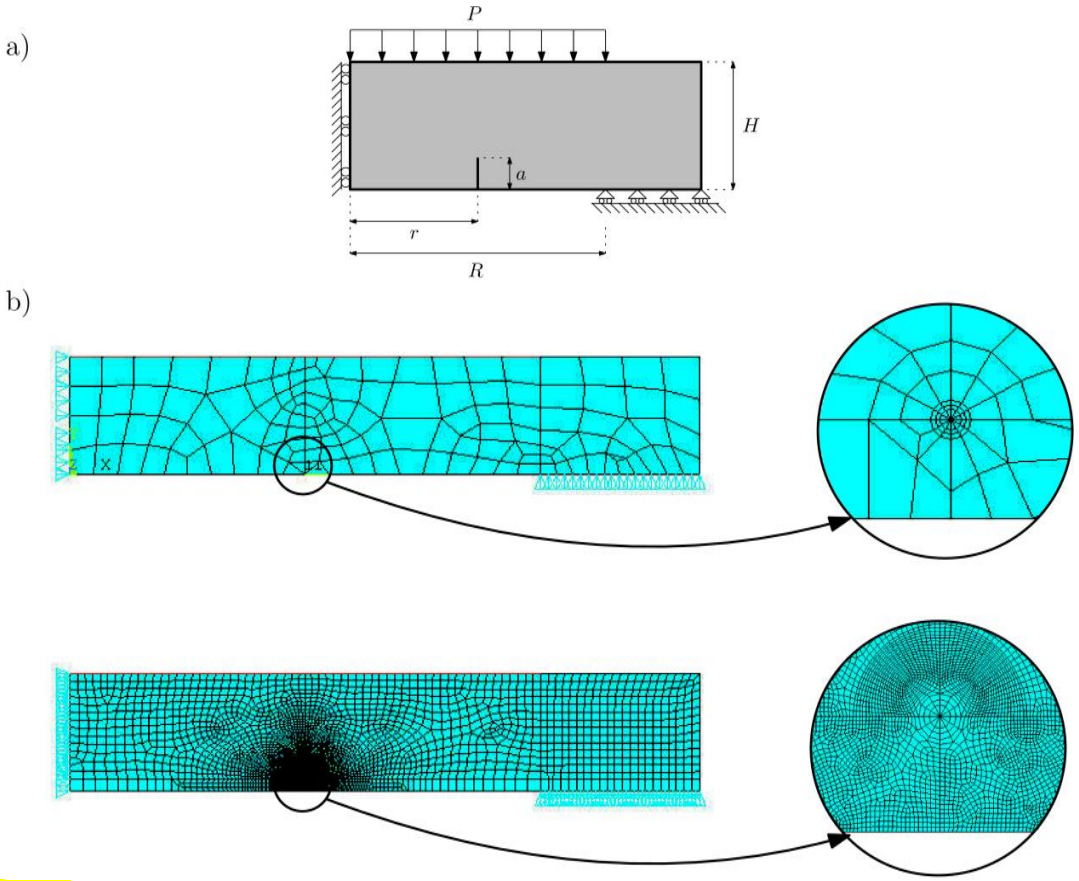

Figure 1: a) Dimensions, load and boundary conditions of the model; b) mesh refinement at the crack tip.

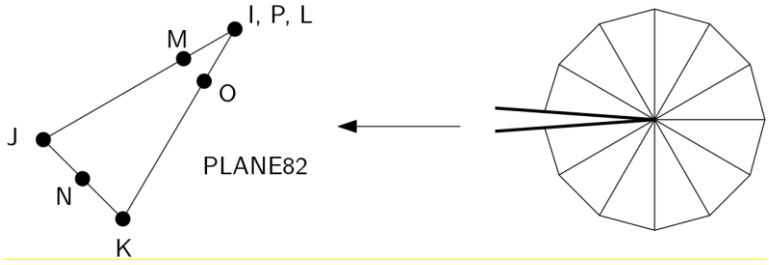

Figure 2: 2D mesh at the crack tip.

The remaining plate geometry was meshed by means of conventional quadrilateral elements of eight nodes. The element size was increased uniformly from the crack tip to the surface of the plate (Figure 1). An iterative mesh refinement process was carried out in order to reduce the mesh discretization error. The target was to meet a stress intensity factor (SIF) increment between two consecutive finer meshes less than 5%. Figure 1 shows two finite element models corresponding to different steps in the mesh refinement process.

The stress field in a plate subjected to bending strongly depends on the material through the Poisson´s ratio ν and, consequently, the SIF values in cracked anchorages are expected to depend on this value.

The plate material in these models was defined as linear elastic with a Young´s modulus E of 200 GPa and a Poisson´s ratio v of 0.4, which is the Poisson´s ratio of polymethyl-methacrylate (PMMA), that was used to check the extent and accuracy of the numerical approach.

For each analysed case, the equivalent SIF at the crack tip was obtained by means of the combination of K_I and K_{II} according to expression (1), which defines a crack propagation criterion when two different modes are present [20]. Values of K_I and K_{II} are obtained by means of the displacement extrapolation technique [21].

$$K_{eq} = (K_I^2 + K_{II}^2)^{1/2} \tag{1}$$

The equivalent SIF is then normalized by the factor K_0 to get a dimensionless value. The value of K_0 is obtained by means of expression (2):

$$K_0 = P\ (\pi a)^{1/2} \tag{2}$$

where P is the applied load on the upper face of the plate.

Figures 3 and 4 permit identifying the effect of the plate thickness H on the SIF. Figure 3 presents the normalized equivalent SIF against the dimensionless depth of the crack a/H for those cracks located at distance $0.5R$ from the symmetric axis. Figure 4 shows analogous results for those cracks located at distance $0.25R$ from the symmetric axis.

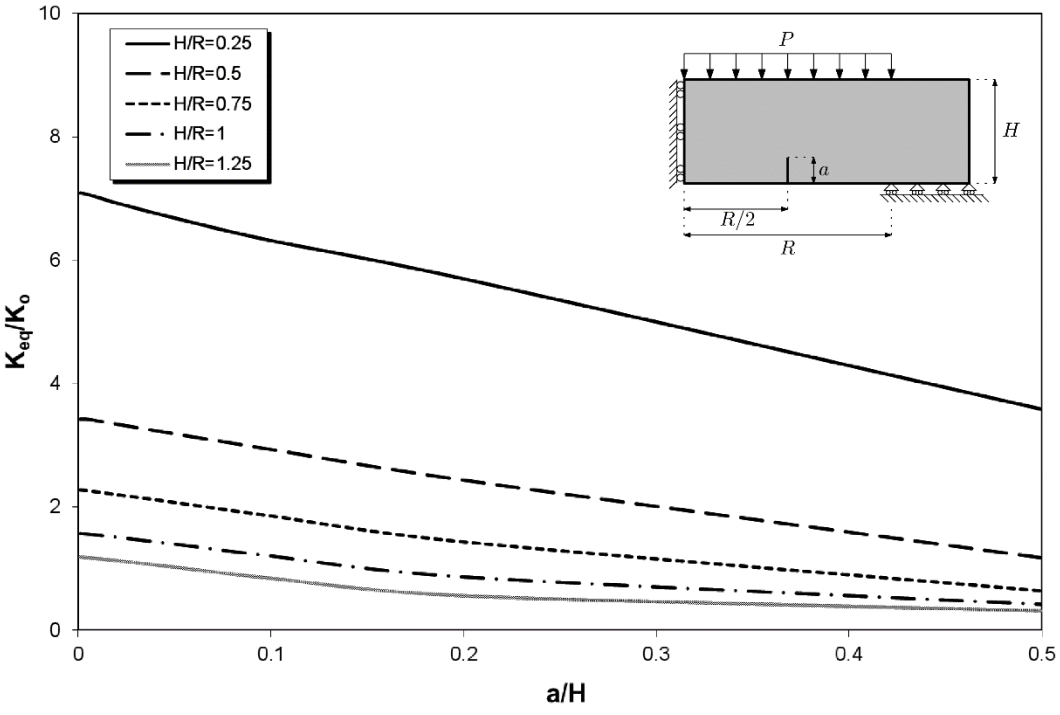

Figure 3: Effect of the plate thickness on the SIF (Cracks placed at R/2).

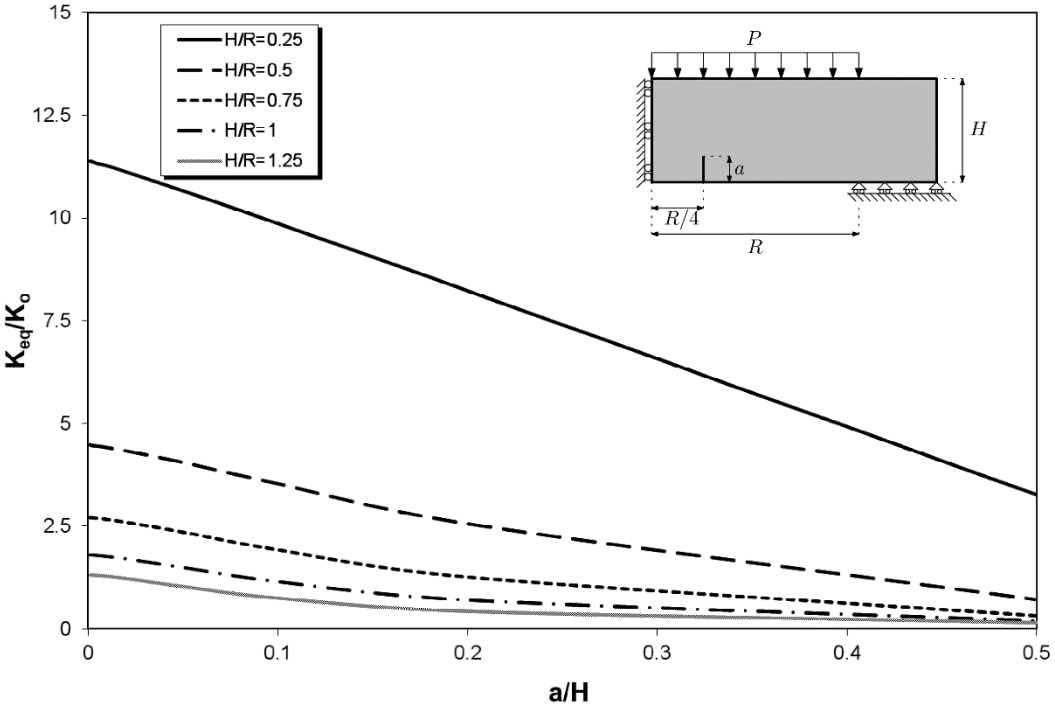

Figure 4: Effect of the plate thickness on the SIF (Cracks placed at R/4).

It can be observed that the smaller the plate thickness *H*, the smaller the damage tolerance for an equal relative depth of the crack *a/H*. When the plate is thicker, part of the load can be directly transferred to the external ring support, which reduces bending in the intermediate region between the symmetry axis and the external support. Since the bending of the plate is what induces tensile stresses at the lower part of the plate, thus opening and propagating cracking, reducing this mechanism leads to a smaller value of SIF, which increases damage tolerance of the plate.

2.2.2. Three-dimensional axisymmetric calculation

A three dimensional calculation with a simple inserted crack was carried out, as shown in Figure 5. The crack had a semi-elliptical shape, with a major semi axis *a* and a minor semi axis *b*. To be consistent with the experimental work, the depth of the crack and the ratio between the major and the minor axis were set to 5.7 mm and 2.6 respectively, which are the average values experimentally measured in tested specimens.

A disc of radius 1.34*R* and thickness *H* is considered, with *R* being the radius of the circular area over which the distributed load *P* is applied (see details at Figure 1). Three values of *H/R* ratio are analysed; *H/R* = 0.25, 0.50 and 0.75. Cracks are located on the tensile side of the plate, at a distance *r* from the symmetric axis of the plate. Three different locations are considered *r*= *R*/2, *R*/4 and 0.88*R*.

The calculation was made with the finite element code ANSYS. Tetrahedral elements of twenty nodes were used in order to generate the finite element mesh.

The mesh at the crack location requires special discretisation due to the stress singularity at the crack tip. Figure 5a shows how the mesh is refined around the crack tip and Figure 5b shows the elements used at the crack tip, which correspond to hexahedral concentric layers with collapsed quarter-point elements at the innermost layer. The crack-front domains were filled with a concentric 20-nodes hexahedral mesh of three layers. Standard elements are used except for the collapsed singular quarter-point elements in the innermost layer connected to the crack-front. This allows obtaining the stress intensity factor by means of the fit of the nodal displacements in the vicinity of the crack tip. The size of the first row of elements was set to 1/10 of the crack depth a in order to give an accurate value of the stress intensity factors (SIF). The number of elements along the crack front was set to keep the aspect ratio of the elements within acceptable values and avoid numerical problems.

The remaining plate geometry was meshed by means of conventional quadrilateral elements of eight nodes. The element size was uniformly increased from the crack tip to the surface of the plate.

The plate material in FE models was assumed as linear elastic with a Young´s modulus E = 200GPa and a Poisson´s ratio v = 0.4.

a)

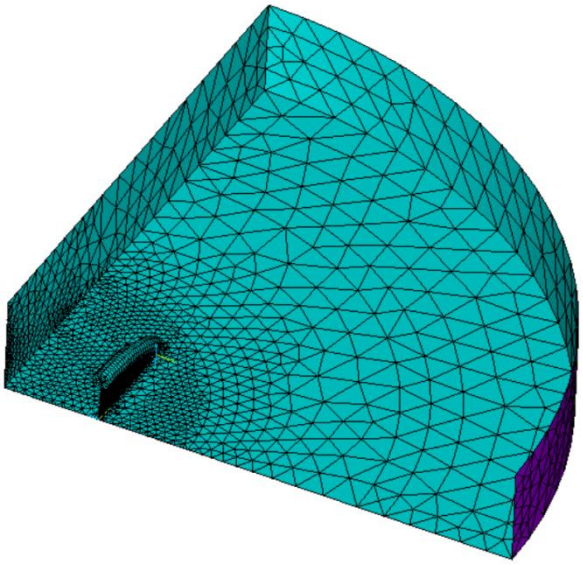

b)

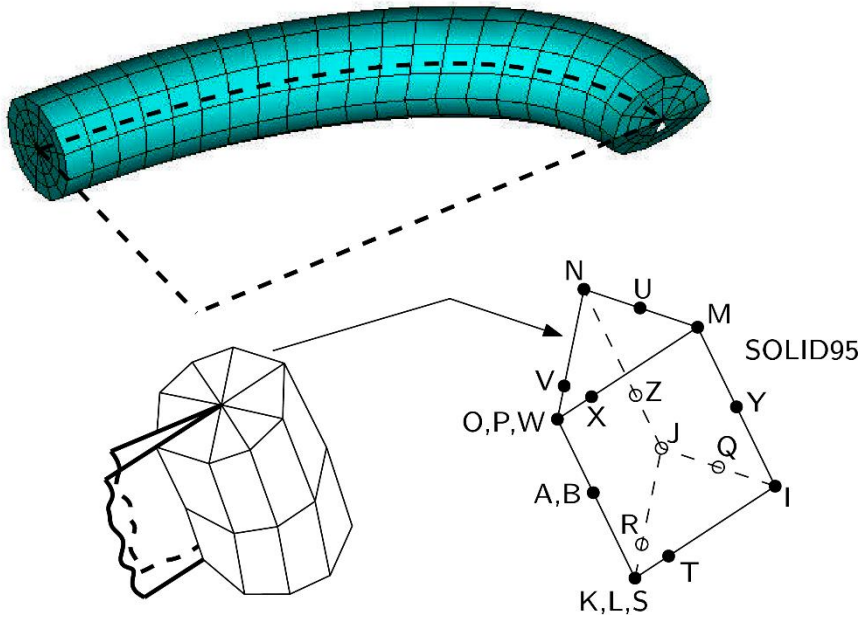

Figure 5: a) Mesh refinement at the crack tip, b) 3D mesh at the crack tip.

Figure 6 shows the resulting SIF (K_I, K_{II} and K_{III}) along the front of the crack for a simple crack in a plate of H/R=0.50 at a distance of $R/2$ from the symmetric axis.

Figure 6 also shows the equivalent stress intensity factor at the crack tip obtained by means of the combination of K_I, K_{II} and K_{III} according to expression (3), which assumes plane strain through the crack front.

$$K_{eq} = \sqrt{K_I^2 + K_{II}^2 + \left(\frac{K_{III}}{1-\nu}\right)^2} \quad (3)$$

The values of K_I, K_{II} and K_{III} as well as the distance of the crack from the external surface edge S are dimensionless, since they have been divided by K_o and the crack front length, respectively.

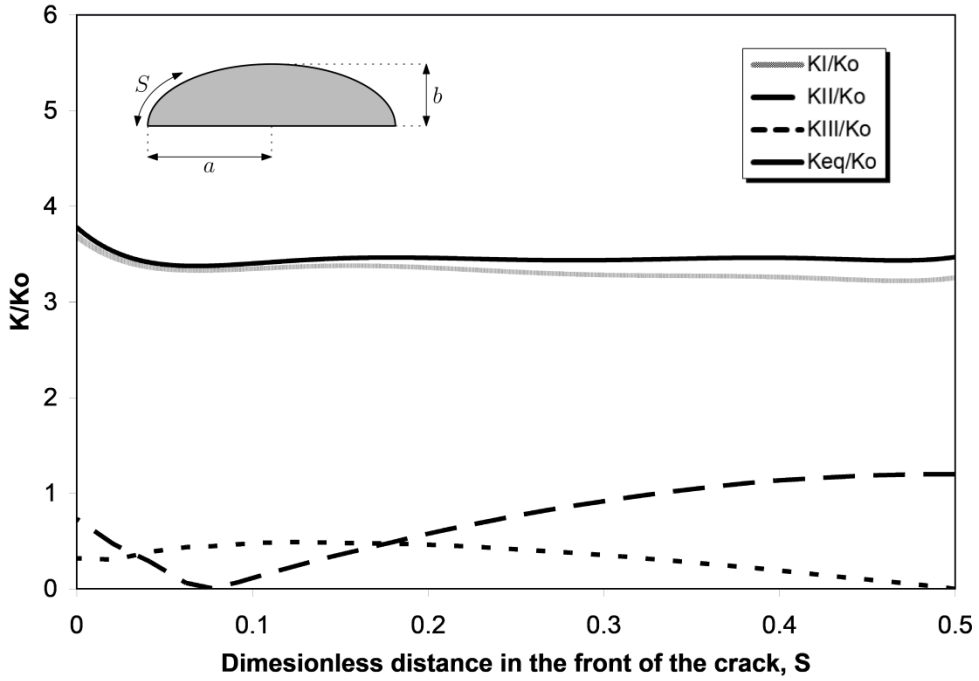

Figure 6: Values of K_I, K_{II} and K_{III} along the crack front (H/R=0.5 with crack placed at $R/2$).

In this case, mode I is clearly dominant and K_{eq} is almost uniform (Iso-K) along the crack front showing a slight increment at the crack edge. Similar results were obtained for those cracks located at $r = R/2$ and $R/4$ regardless of the plate thickness H.

Figure 7 shows the influence of the plate thickness H and the crack location on the SIF. It displays the peak equivalent SIF along the crack front versus the dimensionless distance r/R from the crack location to the symmetry axis. These results show that damage tolerance becomes smaller in thinner plates and with cracks that are closer to the symmetry axis. When a crack enters a region under compression, it stops growing, which happens earlier in the case of thicker plates and when the initial crack is closer to the external ring support. In these cases, part of the distributed load is directly transmitted at the external support and the bending effect becomes reduced, thus relieving tensile stresses at the lower part of the disc, which is responsible for the crack propagation. This is the reason why the curves in Figure 7 become steeper when the plate becomes thinner, since the bending of the plate becomes a more preponderant mechanism, thus inducing faster crack propagation.

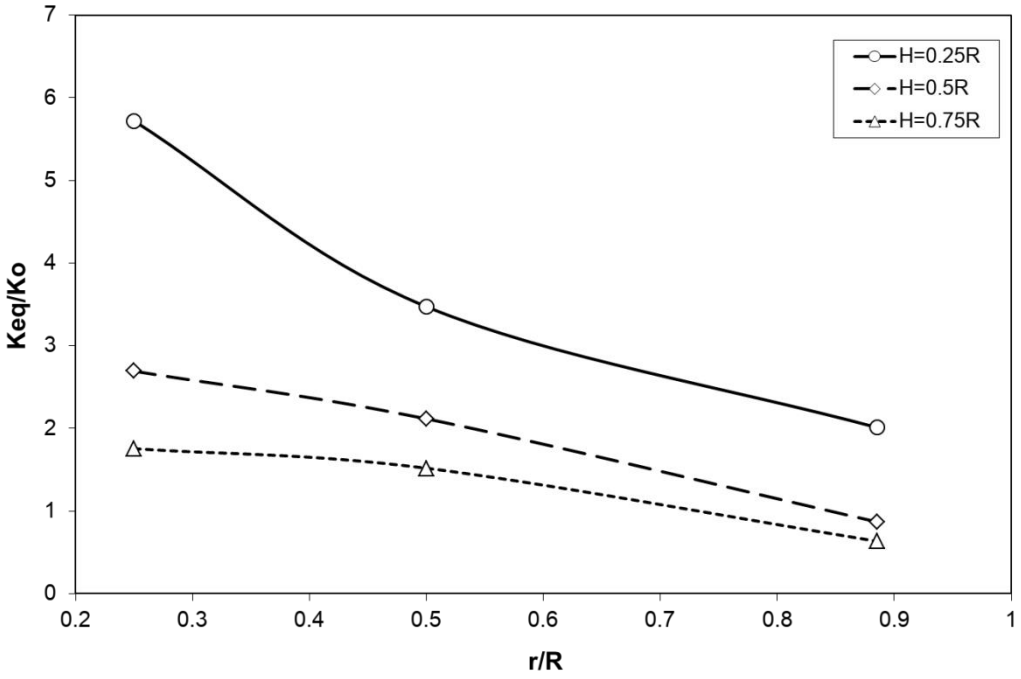

Figure 7: Effects of the plate thickness and the crack location on the SIF.

2.3. A simplified anchor head

The shape of the anchor head was taken from the brochures provided by four manufacturers, with the aim of illustrating a generic pattern, instead of reproducing the specific dimensions and shape of a particular manufacturer. Figure 8 shows the geometry of the anchor head adopted in this research.

The mechanical behaviour of an anchor head is rather complex. Since heavy prestressing loads are applied, many phenomena can be observed: the wedge-tendon gripping action, the friction at the wedge anchor head interfaces, as well as the anchor head-bearing plate interface, among others. Based on the results of previous studies [22, 23], the anchor head is simplified for the numerical analysis. The wedge holes have been suppressed and the load applied by the 31 strands has been evenly distributed on a 102.28 mm radius circle on the anchor head upper face. This circle corresponds to the shut in area by the lower radius circumference which includes all the wedge holes of the anchor head.

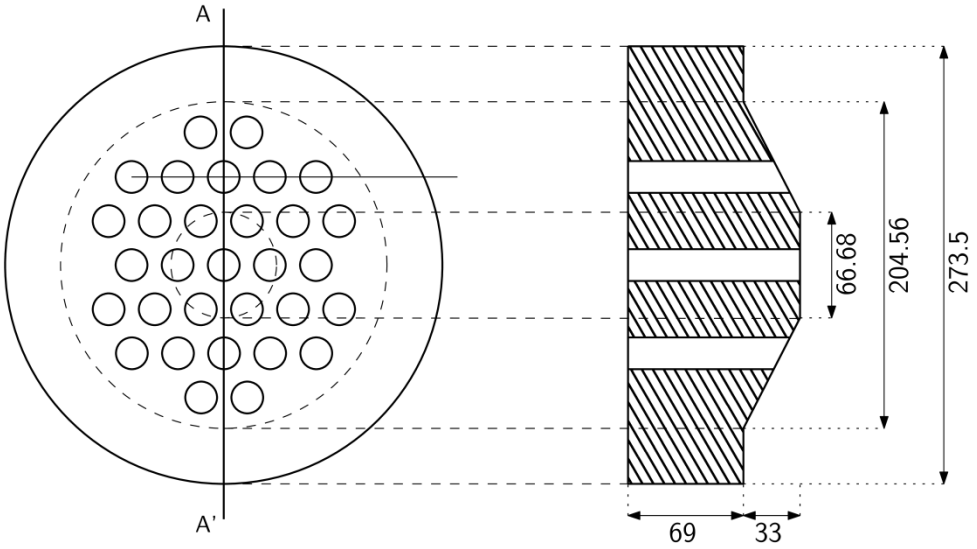

Figure 8: Sketch of the anchor head: geometry and dimensions (in mm).

Again, two types of cracks were taken into consideration; a circular crack and a single crack. Although a circular defect is not very realistic, the fact of making a 2D computation noticeably simplifies the task, especially the production of the finite element mesh, and allows an acceptable analysis of the influence of different variables in a quick and simple way. Furthermore, as will be seen later on, the results provided by this approach lead to a more conservative evaluation of the structural integrity.

2.3.1. Two-dimensional axisymmetric calculation

An anchor head of radius 1.34R and thickness H is considered and six values of H/R are analysed; H/R = 0.25, 0.50, 0.67, 0.75, 1.00 and 1.25. A uniform load P is distributed on a circle of radius R.

Nine different crack sizes are analysed; a/H = 0.001, 0.002, 0.005, 0.01, 0.02, 0.05, 0.1, 0.2 and 0.5. Cracks were placed at the most unfavourable position and orientation which, for an anchor head of radius 1.34R and thickness H/R=0.67 corresponded to the joint zone of the anchor head with an angle of 35° with respect to the anchorage support surface, as it is shown in Figures 9 and 10.

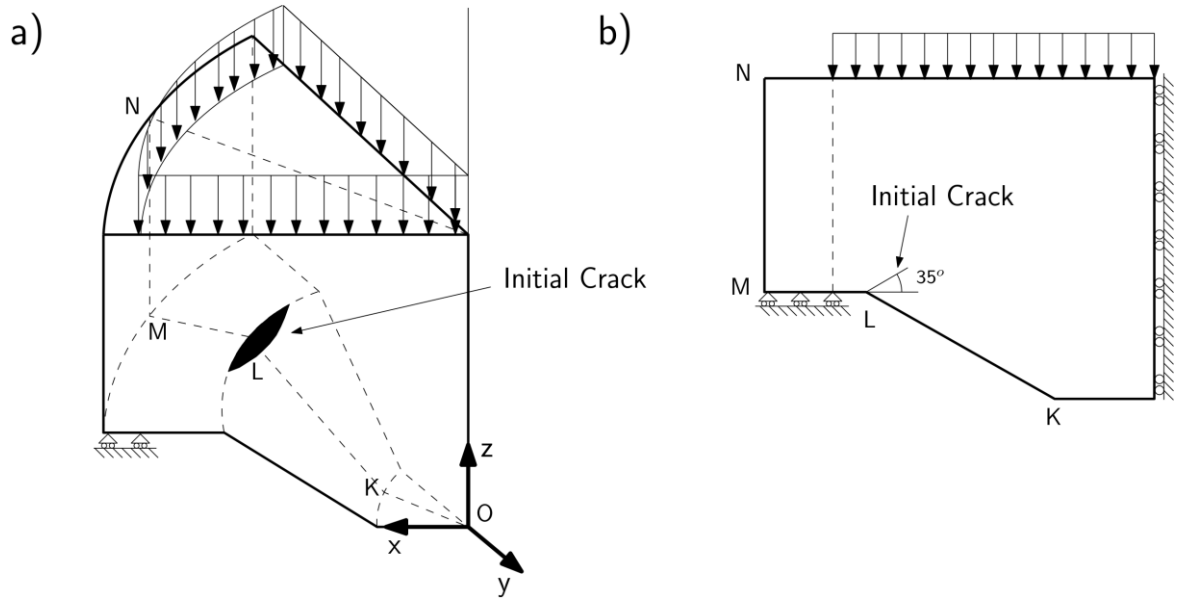

228

229 Figure 9: Shape and location of the initial crack at the anchor head.

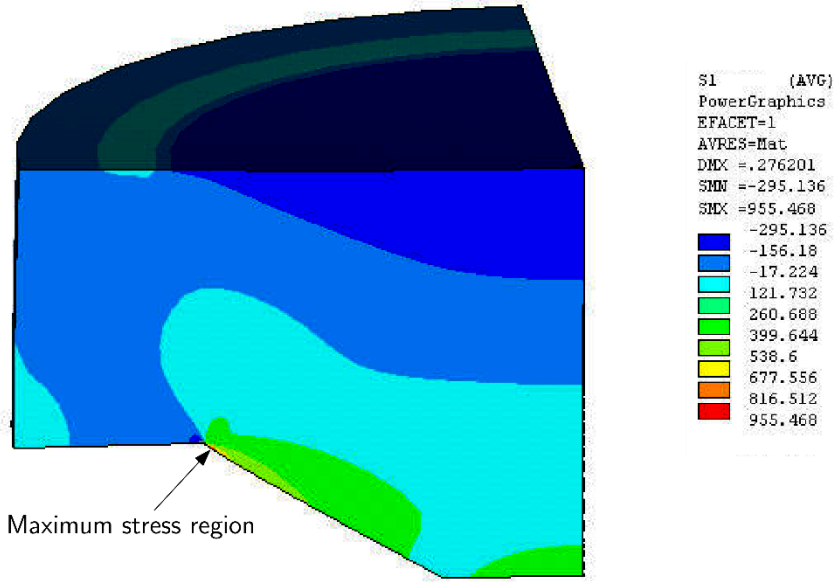

230

231 Figure 10: Linear elastic finite element analysis of stresses in the anchor head.

232 In addition, four different anchor head geometries were analysed to assess the impact of the
233 joint geometry between the cylindrical part of the anchor head and its truncated cone part on
234 the SIF. Three different angles were studied for the joint, θ=90º, 130º and 150º, and a circular
235 joint with radius of 44mm (see Figure 11).

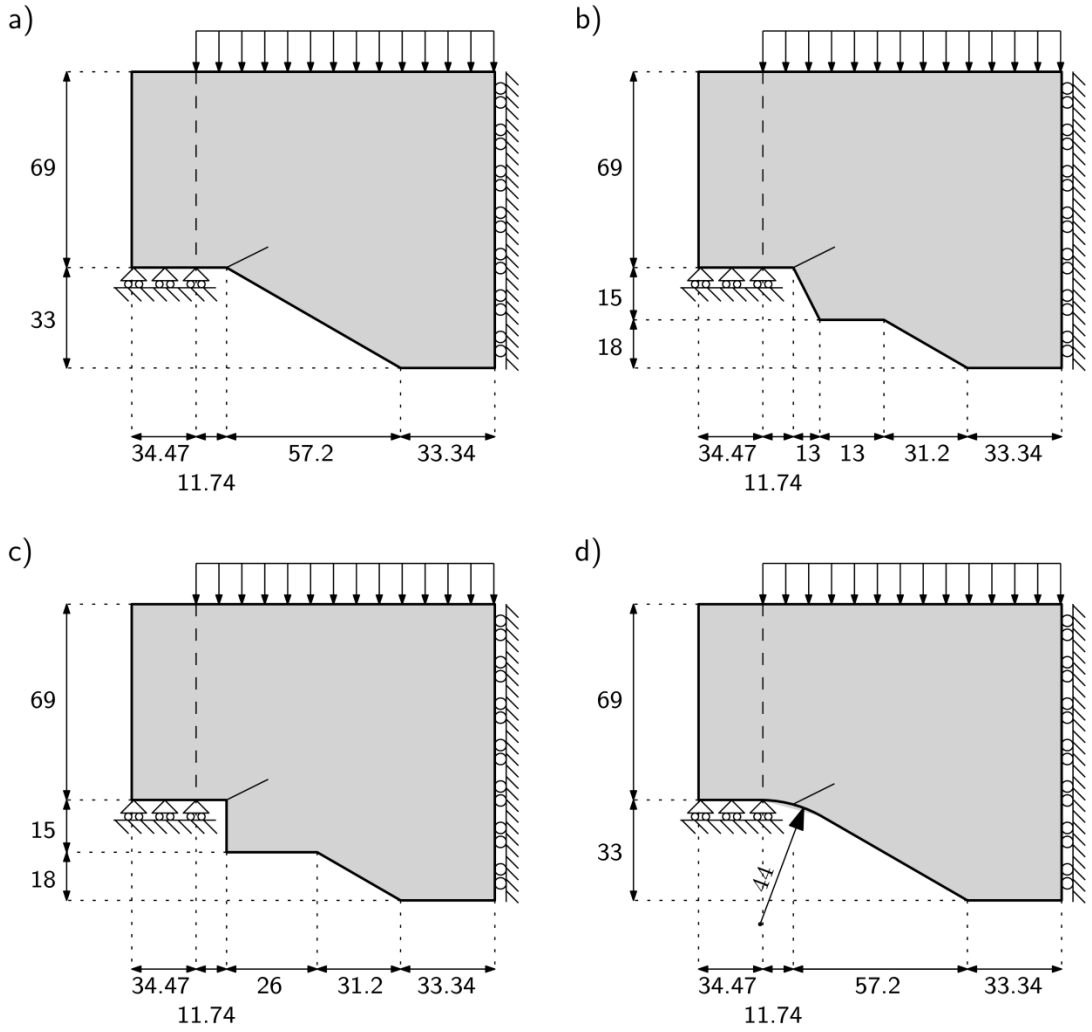

Figure 11: Sketch of different joints in the anchor head analysed in this study: a) θ=150º, b) θ=130º, c) θ=90º and d) circular joint.

The models were produced by using a similar mesh as described for the finite element model of the plate. The material was assumed as linear elastic with a Young´s modulus of 200GPa and a Poisson´s ratio of 0.4.

Figure 12 shows the effect of the anchor head thickness *H* on the SIF. This figure displays the normalized equivalent SIF against the dimensionless depth of the crack *a/H* for all analysed cracks.

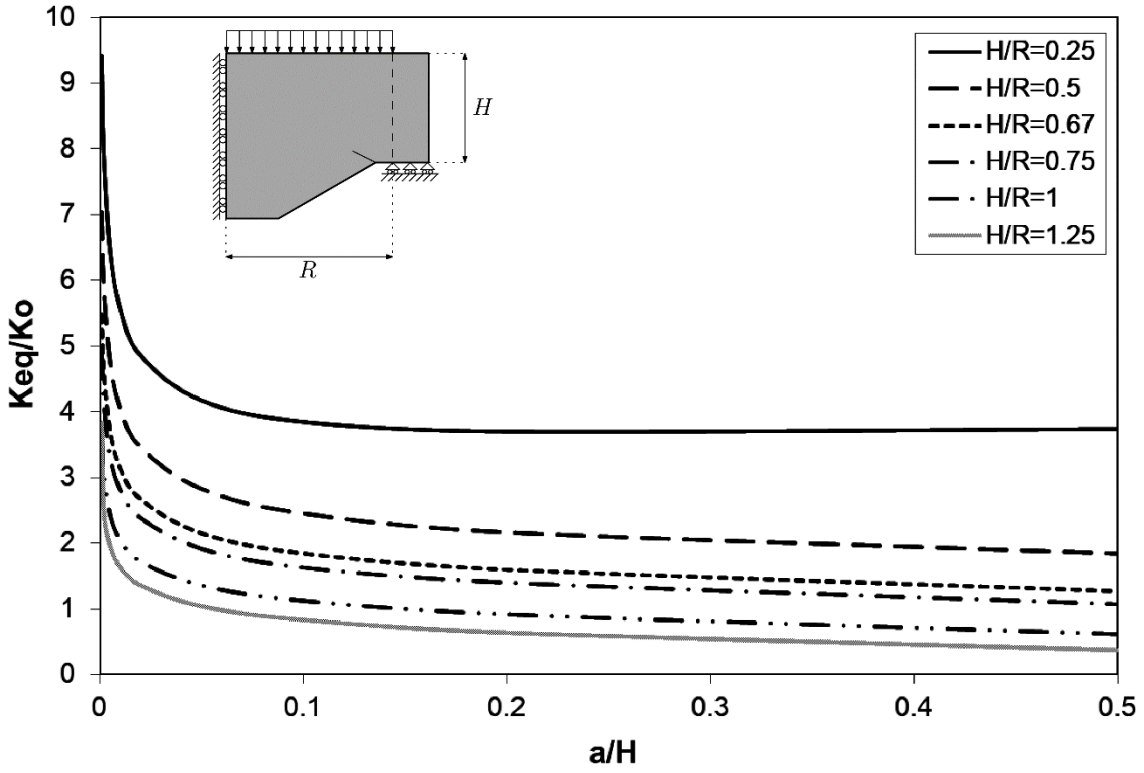

Figure 12: Effect of the anchor head thickness on the SIF.

The results are consistent to those obtained with the analysis of the plate. When the anchor head thickness reduces, the damage tolerance becomes smaller, thus turning the anchorage into a more prone to damage element.

Figure 13 shows the effect of the joint geometry on the SIF. It displays the normalized equivalent SIF against the dimensionless depth of the crack *a/H* for all analysed cracks. The effect of the joint geometry on the SIF is significant for small cracks with ratios of *a/H* less than 0.1; in these cases, SIF reduces when the joint angle is larger, thus increasing the damage tolerance of the anchorage head. On the other hand, the effect of the joint geometry is not relevant when cracks are big enough, since the SIF becomes similar in all cases when the *a/H* ratio is large enough. Therefore, the effect of the joint shape has a great influence on the damage tolerance of the element under small defects; when the joint angle is larger (see Figure 11a), the stress raiser is reduced in comparison with smaller angles (see Figure 11c), which, as shown in Figure 13, has a strong influence on the value of the SIF, thus leading to more damage tolerant elements. If the thickness transition is soft, in especial, if a circular transition is employed (see Figure 11d), damage tolerance is highly increased in the case of very small cracks as observed in Figure 13.

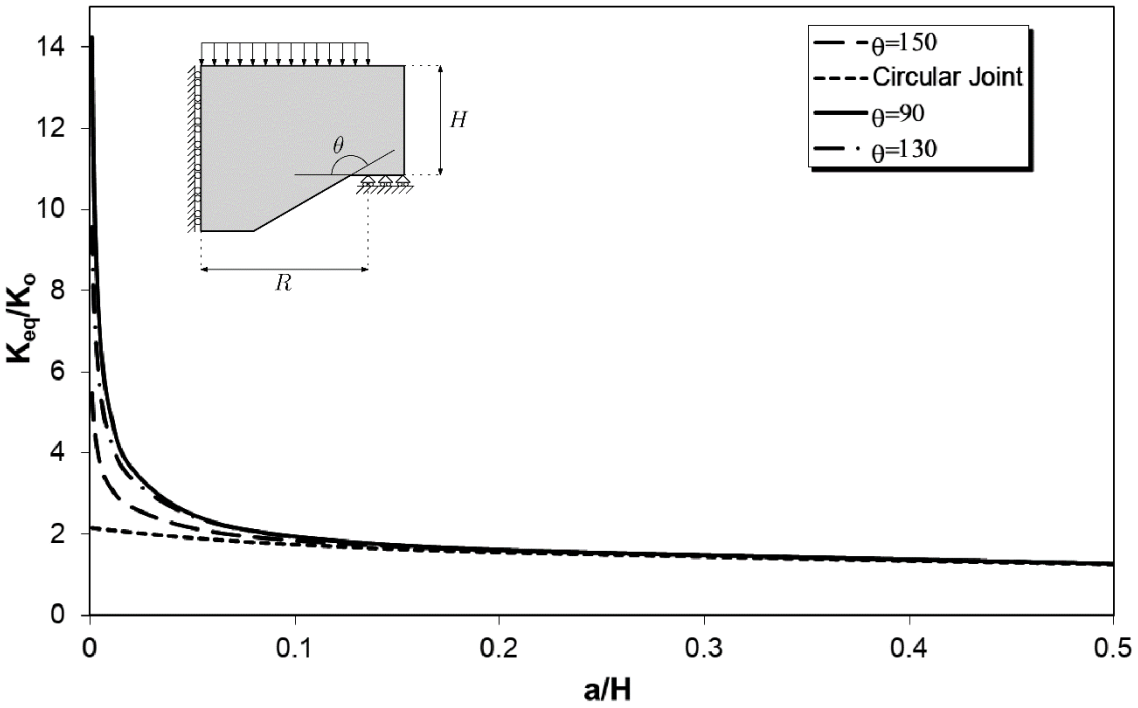

Figure 13: Effect of the joint geometry of the anchor head on the SIF

2.3.2. Three-dimensional calculation

For the single crack, a 3D computation was needed. An anchorage of radius 1.34*R* and thickness *H* is considered. The value of the anchor head thickness *H* was set to 69 mm, which results in a *H/R* ratio of 0.67. A uniform load *P* is distributed on a circle of radius *R*.

The crack had a semi-elliptical shape, with a minor semi axis *a* and a major semi axis *b* (see Fig. 14) and five relations *b/a* were studied: 1, 1.3, 2, 3 and 5, with six values of crack depth *a*: 1, 2, 4, 6, 8 and 10 mm. The relation *b/a* equal to 1.3 was studied because it corresponds to the average measured dimensions of the cracks induced in the experimentally tested PMMA specimens.

Figure 14 shows the resulting normalized SIF (K_I, K_{II} , K_{III} and K_{eq}) along the crack front for a simple crack of 1 mm depth and a relation *b/a* of 1.

For this particular case, mode I is clearly dominant along the crack front. The peak SIF resulted at the surface edge. Similar results were obtained for those cracks with low relations of *b/a*.

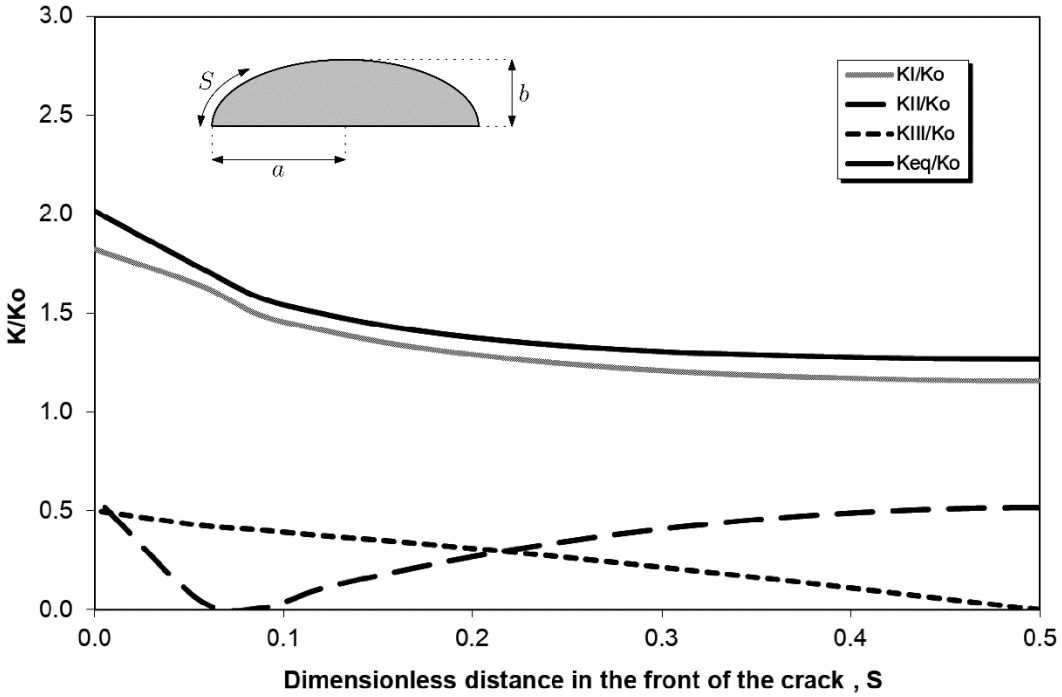

Figure 14: Values of K_I, K_{II} and K_{III} along the crack front (a=1 mm, b/a=1).

Figure 15 shows the equivalent SIF along the front of the crack for a 2mm deep crack and different relations of b/a. In this case, relation $b/a = 2$ approximately leads to a value of an iso-K in the front of the crack. The peak SIF for high relations of b/a shifts from the surface edge to the deepest location of the crack front. Analogous results were obtained with the other crack depths.

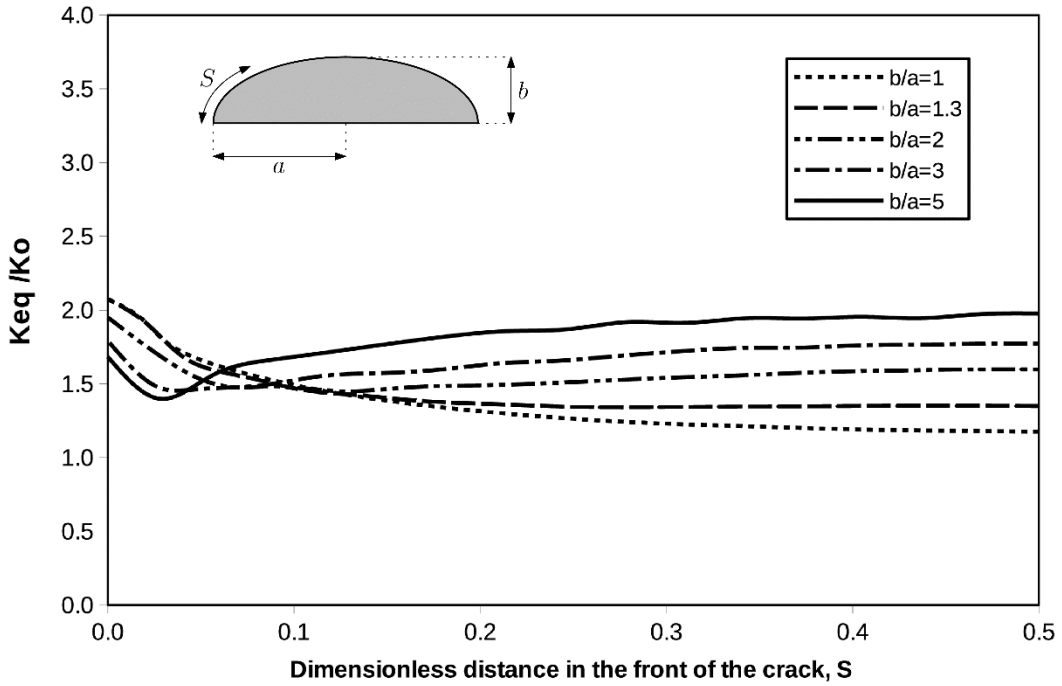

Figure 15: Effect of b/a ratio on the SIF along crack front (a=2mm)

As in the 2D analysis, three different anchor head geometries were analysed to assess the impact of the joint geometry between the cylindrical part of the anchor head and its truncated cone part on the SIF. Three different angles were studied for the joint, θ=90º, 130º and 150º.

For each geometry, a different *b/a* ratio was used. A value of 1.4 was used for those anchorages with a joint of 90º, 1.5 and 1.3 for those anchorages with angles of 130º and 150º respectively. These values were used because they are the average measured values of crack dimensions induced in experimentally tested PMMA specimens.

Figure 16 shows the effect of the joint geometry on the SIF. It displays the peak normalized equivalent SIF along the crack front against the dimensionless depth of the crack *a/H* for all analysed cracks.

The results are analogous to those obtained with the 2D analysis. In the case of small cracks, the equivalent SIF increases when the θ angle is closer to 90º and decreases when it becomes larger, thus increasing the damage tolerance of the element. This is due to the better transmission of stresses at the change of thickness. An abrupt change of thickness, such as that induced by θ=90º, leads to a high stress concentration around the crack, which eases crack propagation. When θ becomes larger and the change of thickness is progressive, the stress concentration is reduced.

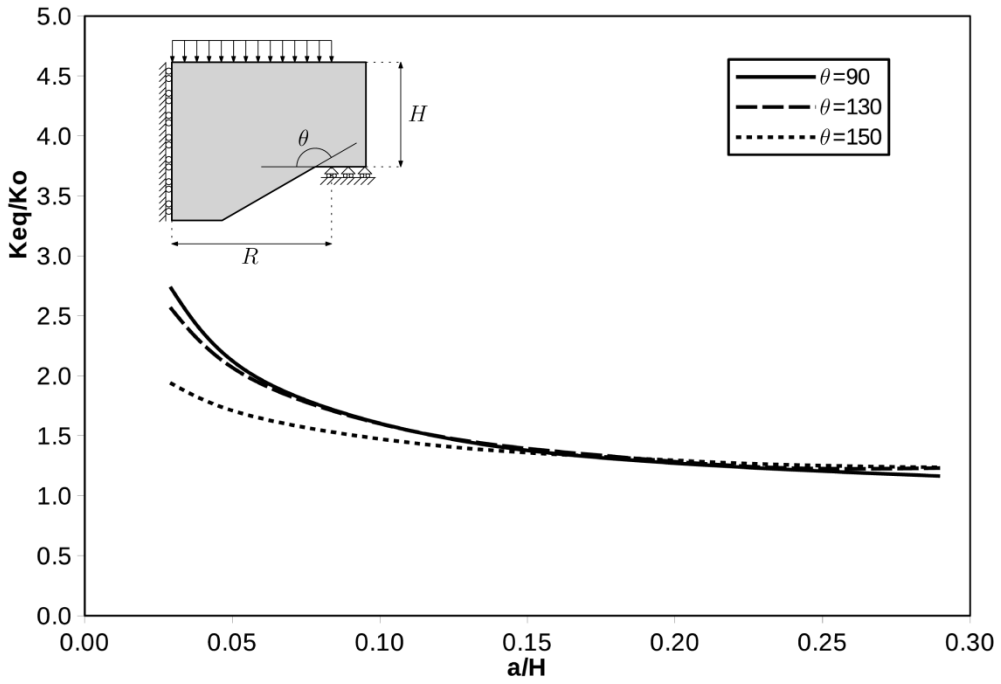

Figure 16: Effect of the joint geometry of the anchor head on the SIF

3. Experimental work

To check the extent and accuracy of the previous numerical approach, an experimental program was carried out. Several anchor heads —some with a disc shape and others with more realistic shapes— were damaged with single cracks and tested until failure.

3.1. Material characterisation

The material chosen for the experimental programme was polymethyl-methacrylate (PMMA), an amorphous glassy polymer that exhibits a quasi-elastic linear behaviour at room temperature, and because of its excellent optical properties, it allows controlling the crack generation process as well as its progression during the test.

Tensile tests, with cylindrical samples, and fracture toughness tests, with notched beams, were performed according to standards [24-27] as described in [17]. The average mechanical properties are shown in Table 1.

Table 1: Average mechanical properties of PMMA

UTS(MPa)	E(GPa)	ν	K_{IC} (MPa $m^{1/2}$)
76.6	2.66	0.42	1.25

3.2. Samples and experimental equipment

Two specimen geometries were tested: circular discs and simplified anchor heads. Shapes and dimensions are shown in Figures 17 and 18.

Both specimen types were manufactured using 1 m long PMMA bars with a diameter of 140 mm. Dimensions of the experimental samples were scaled using a ratio of 1:2 compared with the finite element models in order to adjust them to those of the PMMA bars.

For each anchorage, the crack was generated in two stages; first, a notch was cut with a steel disc of 25 mm diameter and 0.5 mm thickness. In a second step, a crack was made inserting a sharp circular blade and pressing in a controlled way. This wedging effect generates cracks with almost elliptical shapes, which was verified after the tests.

The testing of circular discs was carried out to assess the effect of the plate thickness H and the location of the crack on the damage tolerance of the anchor head. Single cracks were placed in circular discs at three different locations at distance r from the symmetry axis. Single cracks of similar dimensions were placed with its plane normal to the anchorage support surface. Three sets of six circular plates were manufactured combining three thicknesses, 12.785, 25.57 and 38.355 mm, and three crack locations, r = 12.785, 25.56 and 45.27 mm.

The analysis of different anchor head geometries shown in Figure 11 suggest that the angle θ (see Figure 13) may play a relevant role in the fracture behaviour of the anchor head. Three sets of six anchorages were prepared in order to assess the effect of the joint geometry between the cylindrical part of the anchor head and its truncated cone part on the damage tolerance; one with θ = 90˚, (anchorage type A90), one with θ = 130˚, (anchorage type A130) and another one

with θ = 150˚ (anchorage type A150). Single cracks of different sizes were placed in the most unfavourable zone with its plane oriented 35° with respect to the anchorage support surface.

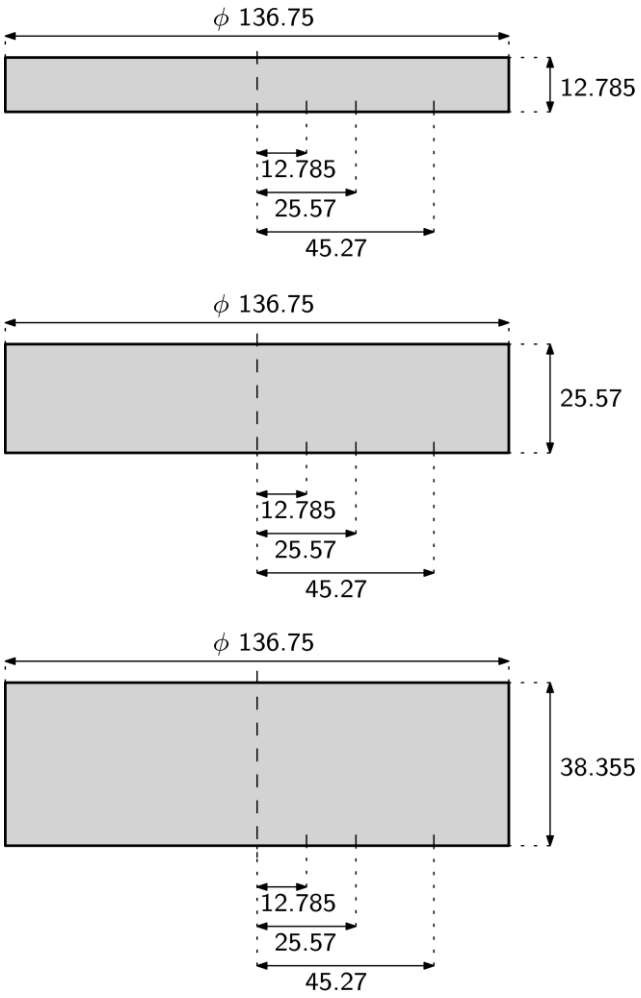

Figure 17: Circular plate sample geometries (distances in mm).

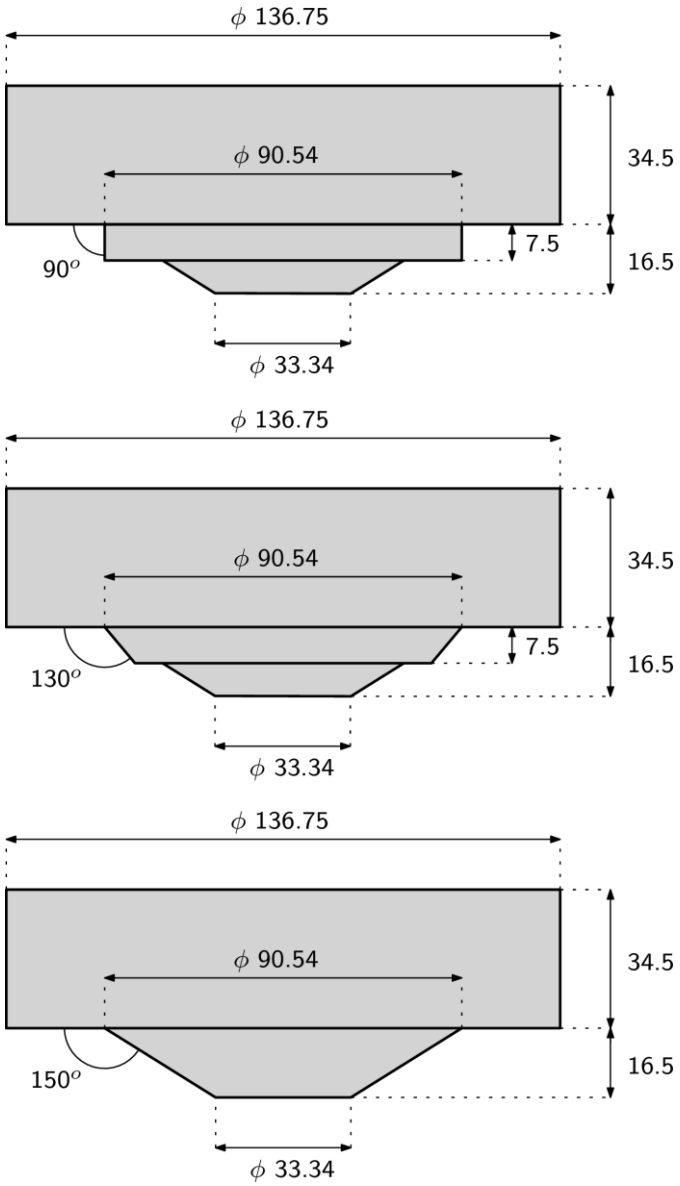

Figure 18: Anchorage sample geometries(distances in mm).

The experimental setup is shown in Figure 19. The anchor head was supported on an external ring to reproduce the boundary conditions used in the numerical analysis; this boundary was lubricated to diminish the friction forces; it must be noted that friction could make results more similar to actual on-site cases, but in this study lubrication permits easier comparison with the numerical results. The load actuator applied a uniform pressure upon a circular surface on the specimen. An elastomeric disc of 10 mm thickness was placed between the actuator and the anchorage to evenly distribute the load.

During the test, the applied load, the vertical displacement of the load application point (extensometer LVDT 1), the vertical displacement of the anchorage lower face central point (LVDT 2) and the possible lifting of the anchorage edges in the support, measured in two diametrically opposed points (extensometers LVDT 3), were continuously recorded.

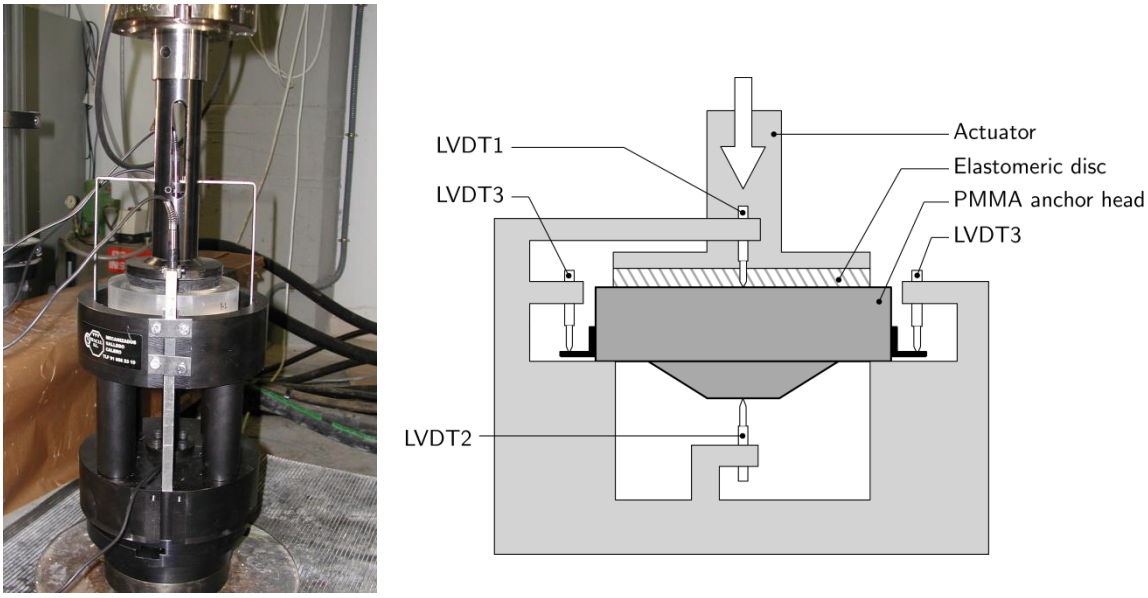

Figure 19: Experimental setup.

3.3. Experimental results

Tests were made under displacement control of the load actuator with a speed of 0.4 mm/min. During the test, the extensometers LVDT 3 in Figure 14 did not detect any movement, as was hypothesized in the numerical simulation.

The initial crack dimensions were measured at the fractured samples after the tests; these values are presented in Tables 2 and 3.

Table 2: Circular plate geometry and crack dimensions measurements.

Sample	H (mm)	Crack location r (mm)	a (mm)	$2b$ (mm)	b/a
H12.1	12.8	46.7	4.90	30.00	3.06
H12.2			6.14	28.40	2.31
H12.3		34.0	4.90	28.80	2.86
H12.4			4.82	30.40	3.15
H12.5		12.2	4.40	29.02	3.30
H12.6			5.94	30.00	2.53
H25.1	25.6	47.2	7.60	29.50	1.94
H25.2			7.20	30.50	2.12
H25.3		24.2	5.46	29.30	2.68
H25.4			6.00	30.30	2.53
H25.5		12.2	4.86	29.60	3.05
H25.6			5.14	29.10	2.83
H38.1	38.3	43.8	6.22	29.76	2.39

H38.2			6.18	26.20	2.12
H38.3		23.5	6.30	30.04	2.38
H38.4			5.72	29.60	2.59
H38.5		11.6	5.64	31.10	2.76
H38.6			5.00	30.10	3.01

368

369 Table 3: Crack dimensions measurements in anchor heads.

Sample with θ =150°	*a*(mm)	*b*(mm)	*b/a*
A90.P1	3.18	5.16	1.62
A90.P2	4.29	5.70	1.33
A90.P3	4.42	6.64	1.50
A90.P4	4.69	6.64	1.42
A90.P5	6.20	8.60	1.39
A90.P6	6.75	9.15	1.36
A130.P1	3.49	5.44	1.56
A130.P2	3.48	5.43	1.56
A130.P3	4.69	6.99	1.49
A130.P4	4.20	6.81	1.62
A130.P5	5.01	7.36	1.47
A150.P1	3.33	4.36	1.31
A150.P2	3.44	4.83	1.41
A150.P3	4.43	6.27	1.42
A150.P4	4.71	6.43	1.36
A150.P5	4.79	6.08	1.27
A150.P6	6.10	7.01	1.15

370

371 The ultimate load was recorded for every single test. Ultimate loads for the two sets of samples
372 are drawn in Tables 4 and 5; the crack depth of every sample is also provided in order to
373 facilitate the analysis of the experimental results.

374 Table 4: Ultimate loads for circular plate samples.

Sample	Crack depth (mm)	Ultimate load (KN)
H12.1	4.90	57.0
H12.2	6.14	59.0
H12.3	4.90	27.1
H12.4	4.82	28.4
H12.5	4.40	20.9
H12.6	5.94	20.1
H25.1	7.60	101.4

H25.2	7.20	106.0
H25.3	5.46	36.3
H25.4	6.00	35.1
H25.5	4.86	30.7
H25.6	5.14	31.4
H38.1	6.22	182.6
H38.2	6.18	185.0
H38.3	6.30	69.2
H38.4	5.72	70.7
H38.5	5.64	58.2
H38.6	5.00	59.5

375

376 Table 5: Ultimate loads for anchor head samples.

Sample	Crack depth(mm)	Ultimate load (KN)
A90.P1	3.18	95.0
A90.P2	4.29	75.5
A90.P3	4.42	88.7
A90.P4	4.69	72.6
A90.P5	6.20	78.0
A90.P6	6.75	76.0
A130.P1	3.49	99.06
A130.P2	3.48	128.1
A130.P3	4.69	109.54
A130.P4	4.20	106.47
A130.P5	5.00	129.61
A150.P1	3.33	118
A150.P2	3.44	134.8
A150.P3	4.43	109.6
A150.P4	4.71	118.0
A150.P5	4.79	130.0
A150.P6	6.10	105.0

377

378 Figure 20 shows the influence of plate thickness *H* and the location of the crack; as the
379 thickness of the circular plate increases, breaking load increases, as expected. The influence of
380 crack locations - through distance *r* from the symmetry axis - is clearly observed, since breaking
381 loads in those cases with cracks closer to the symmetry axis are much lower than those with
382 cracks located further.

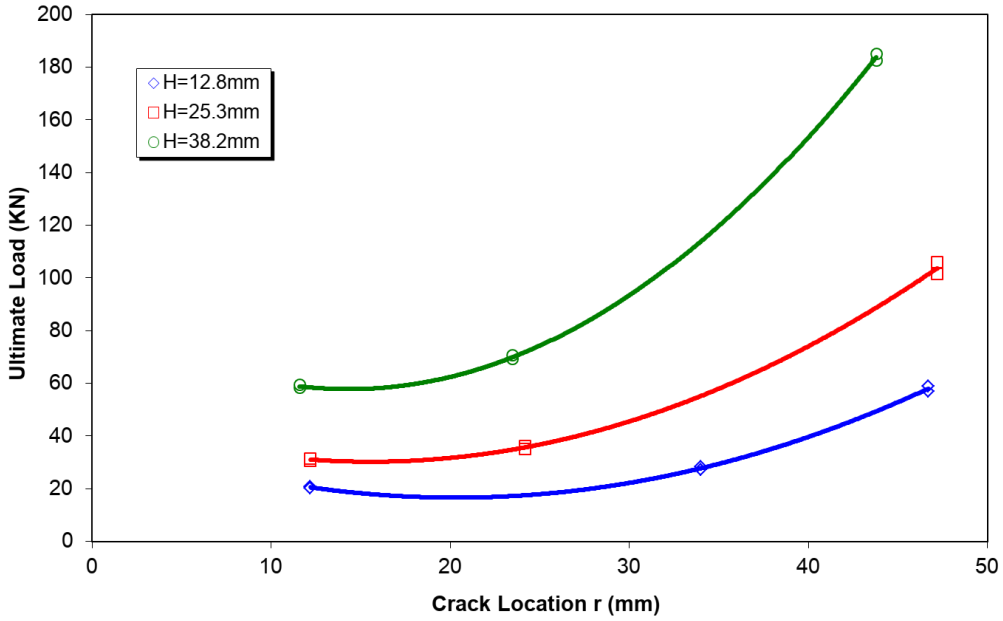

Figure 20: Effects of thickness and crack location on ultimate loads in circular plate samples.

Figure 21 shows the influence of crack depth on the breaking loads of anchor head samples; as the crack size increases, breaking loads —on average— decrease. The influence of anchor head shape —through angle θ— is clearly observed, as breaking loads for sharp transitions are much lower than for smooth ones. This can be explained in terms of stress concentration at the change of the plate thickness, as mentioned before, which is more abrupt when θ=90º and more progressive when θ=150º.

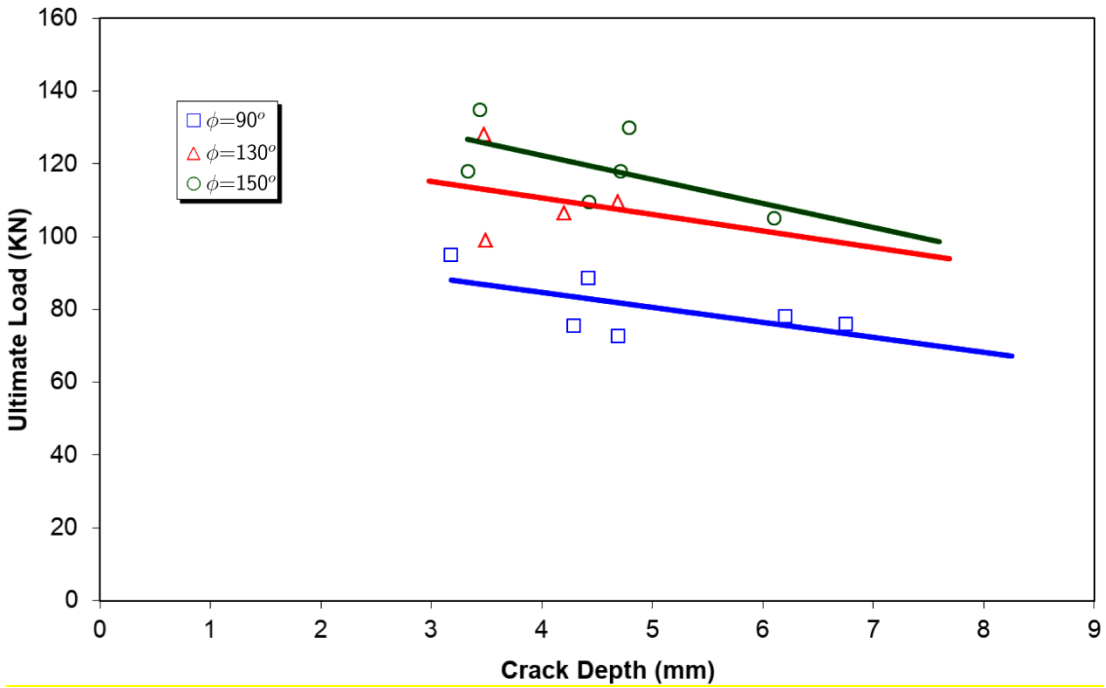

Figure 21: Effects of joint geometry and crack depth on ultimate loads in anchorage samples.

3.4. Comparison with numerical predictions

Predicted breaking loads from the numerical models were derived from the resulting stress intensity factors by means of a local fracture criterion by matching the equivalent stress intensity factor with the experimentally obtained fracture toughness:

$$K_{eq} = \sqrt{K_I^2 + K_{II}^2 + \left(\frac{K_{III}}{1-\nu}\right)^2} = K_{IC} \quad (3)$$

Figure 22 shows the fit of the experimental breaking loads with the predictions derived from the 2D and 3D finite element models of circular plates. As shown in Figure 22, the fit of the experimental points with the numerical predictions is good for plates of 12.8 and 25.6mm thickness and with cracks located closer to the axisymmetric axis (r=R/2 & R/4). However, the fit of experimental points is not so good in the case of thicker plates, H=38.6 mm, with cracks located further from the axisymmetric axis (r=0.88R).

The influence of defects on the performance of the plates can be roughly evaluated by comparing the experimental values of a cracked plate with an estimation of the breaking load of a plate without defects. Using finite element models of circular plates without cracks and a fracture criterion based on the maximum stress (Rankine criterion), the breaking load was estimated for each circular plate. Figure 22 also shows the breaking loads of defect-free plates which were derived using these 2D models. As can be observed, the experimental breaking load for the thinner (H=12.8mm) and with a crack at the furthest studied location (r=0.88R) is close to the value predicted by Rankine criterion. For the thicker plates, the experimental values are much lower than those predicted by Rankine criterion.

Numerical models predict reasonably well the effect of plate thickness and the crack location, since breaking loads agree with the experimental results. It should be noted that no significant discrepancies were found between the 2D and 3D breaking load predictions, therefore, 2D models can be recommended in axisymmetric cases, since they result in much simpler to build models and easier to interpret results.

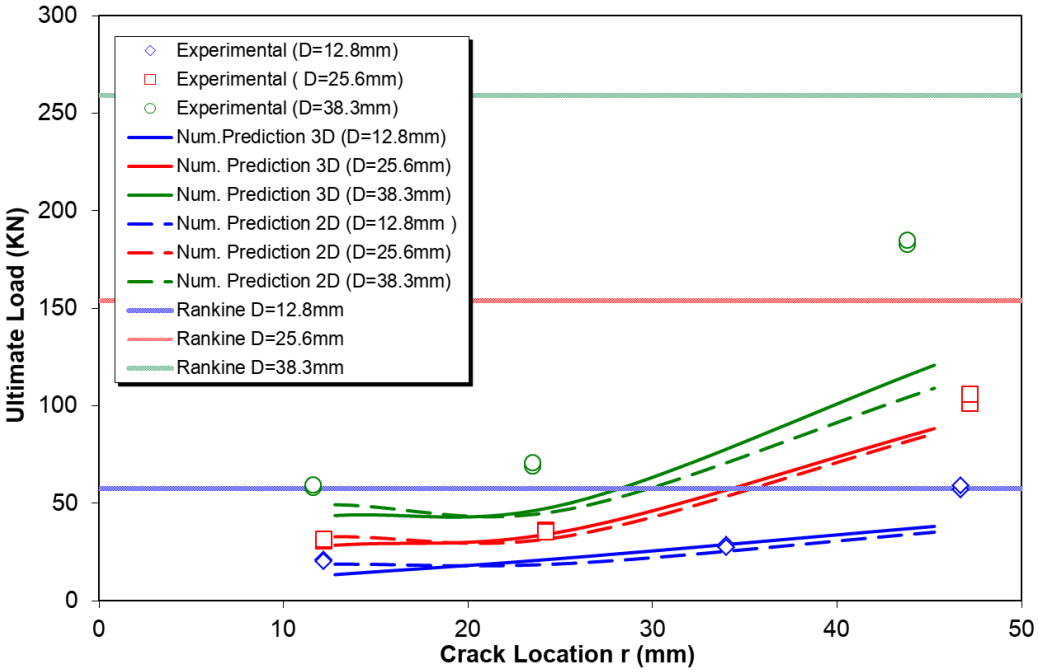

Figure 22: Fit of experimental breaking loads to predictions for circular plates.

Figure 23 shows the fit of the experimental breaking loads with the numerical predictions derived from the results obtained with the finite element models of anchor heads. As shown in Figure 23 the fit of the experimental results with the numerical predictions is not very good for the three different anchor head samples which were tested.

Significant discrepancies were also found between the 2D and 3D numerical predictions of the breaking load. Numerical predictions derived from two dimensional axysimmetric models were found conservative.

Figure 23 shows the theoretical breaking loads of defect-free anchorages which were derived by means of the Rankine failure criterion from 2D models of defect-free anchorages. As can be observed, the experimental values of the three tested sample geometries are much lower than those predicted by the Rankine criterion.

Numerical models predict reasonably well the effect of the crack size and the joint geometry on the breaking load of anchorage samples. Numerical results predict a decrease of the breaking load when the crack depth increases. The slope of the curves shown in Figure 23 is flatter for the range of tested crack sizes than that for smaller cracks with depths below 1mm. Hence, the effect of the tested crack sizes on breaking load is less significant than the effect expected for cracks with depths below 1 mm. However, numerical results derived from the 2D and 3D models predict no differences on breaking loads between the different joint geometries for cracks with depths around 4 and 5 mm. This prediction is not consistent with the test results on which differences in breaking loads were found for the whole range of tested crack sizes.

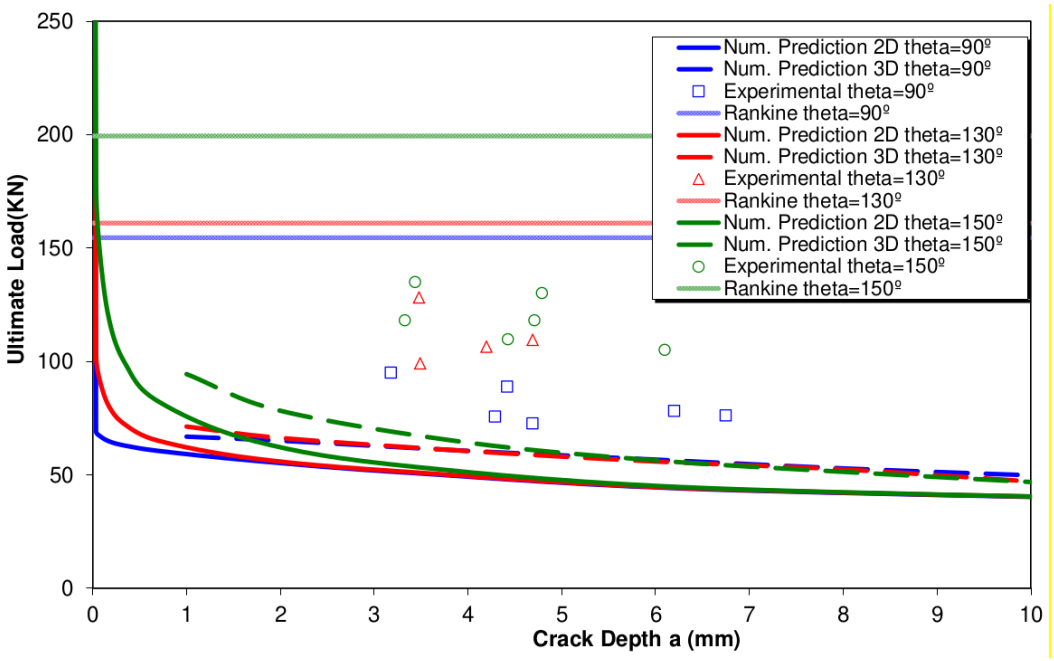

Figure 23: Fit of experimental breaking loads to predictions for anchorages.

These results are consistent with those obtained for circular plates, because the thickness and crack location of the anchorage samples are similar to those of the circular plate samples which showed the more deficient fit with the experimental results.

Damage location on anchor head specimens is very close to the contact face between the specimen and the supporting annular ring, therefore the boundary conditions applied on these locations could have an impact on the results. In the finite element models, the nodal displacement at contact faces were restricted in the normal direction and no restrictions were applied in other directions.

In order to better reproduce the test conditions, the supporting ring was also considered into the 2D finite element models. The contact between the specimen sample and the supporting ring was modelled by means of contact elements at the interface assuming a friction coefficient of 0.5 between PMMA and steel which is in line with the values found in literature [28].

In the case of 3D models, in order to simplify their performance and avoid numerical problems, instead of modelling the contact between the specimen and the supporting ring, the displacements resulting from the 2D analysis were used as input in the 3D models of damaged specimens. This allowed calculating the stress intensity factors to derive the breaking loads for the range of analysed crack sizes.

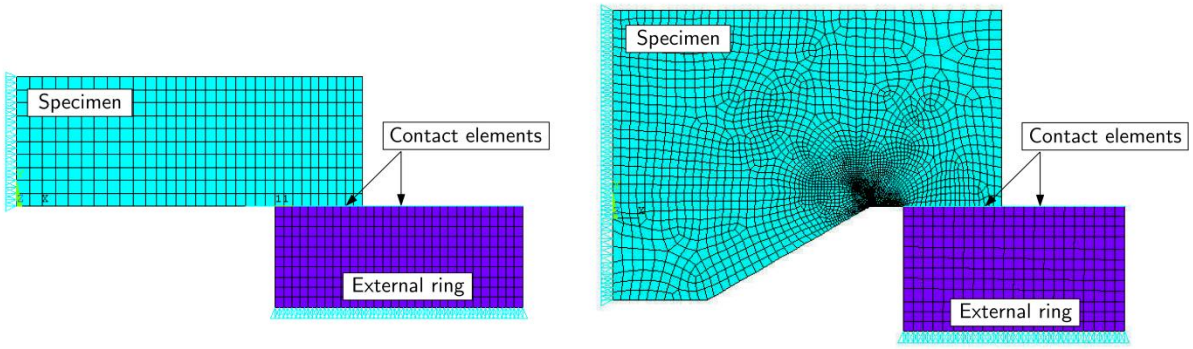

459

460 Figure 24: 2D finite element models including the effect of friction at the interface.

461 Figures 24 and 25 show the influence of friction on the breaking loads of anchor head and
462 circular plate samples. The experimental breaking loads of anchorage samples are placed
463 between both predictions with and without friction.

464 a)

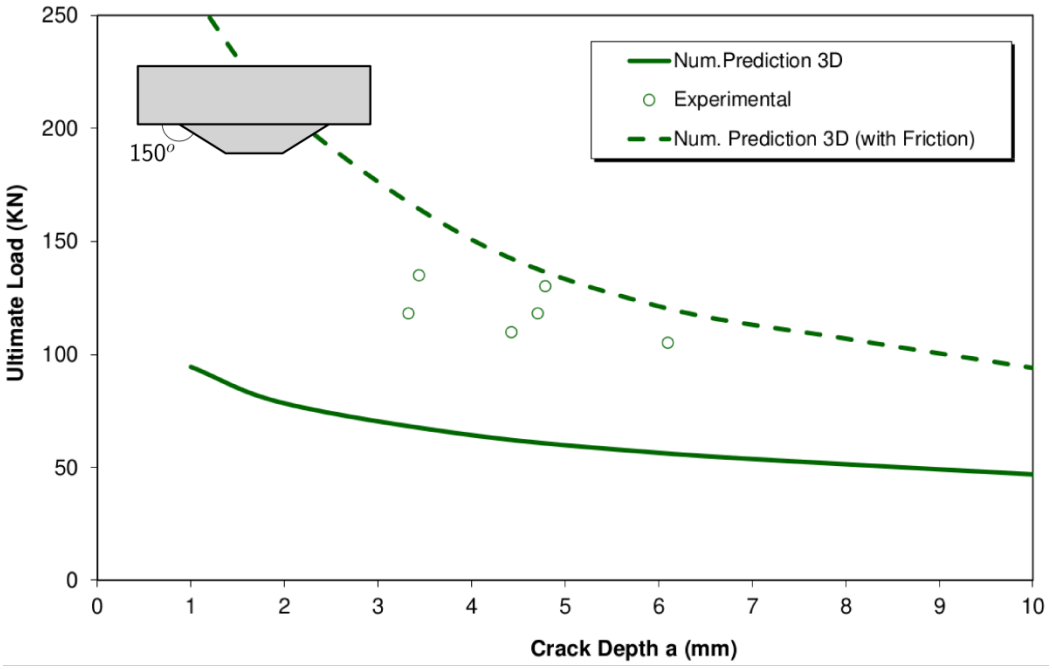

465

466 b)

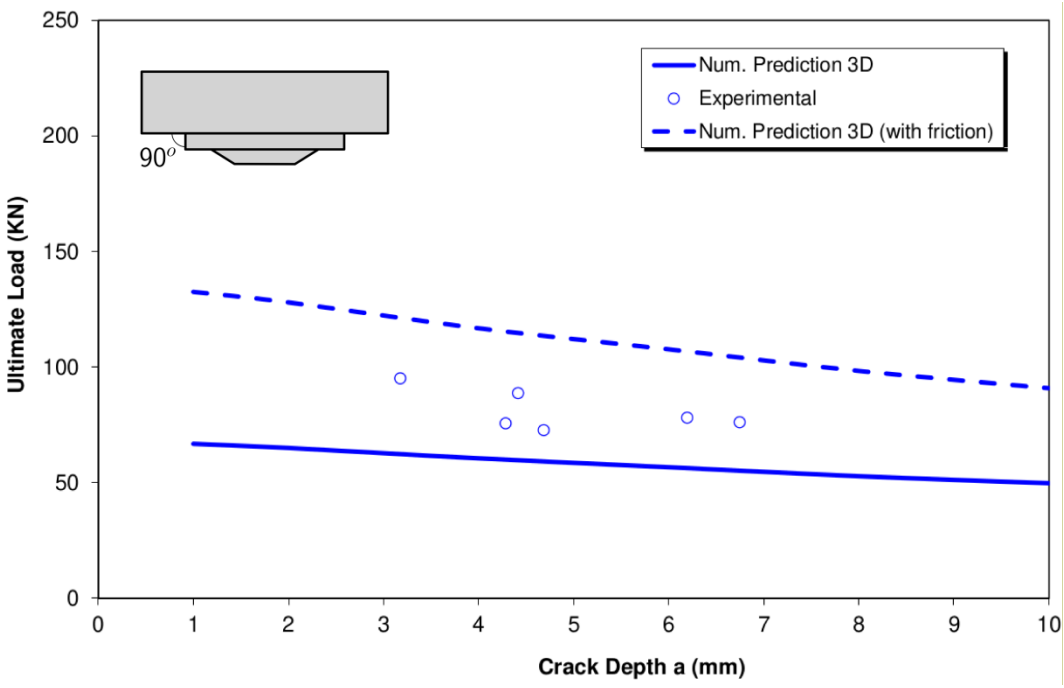

Figure 25: Effect of friction on breaking loads in anchorage specimens: a) specimens with θ=150º, b) specimens with θ=90º.

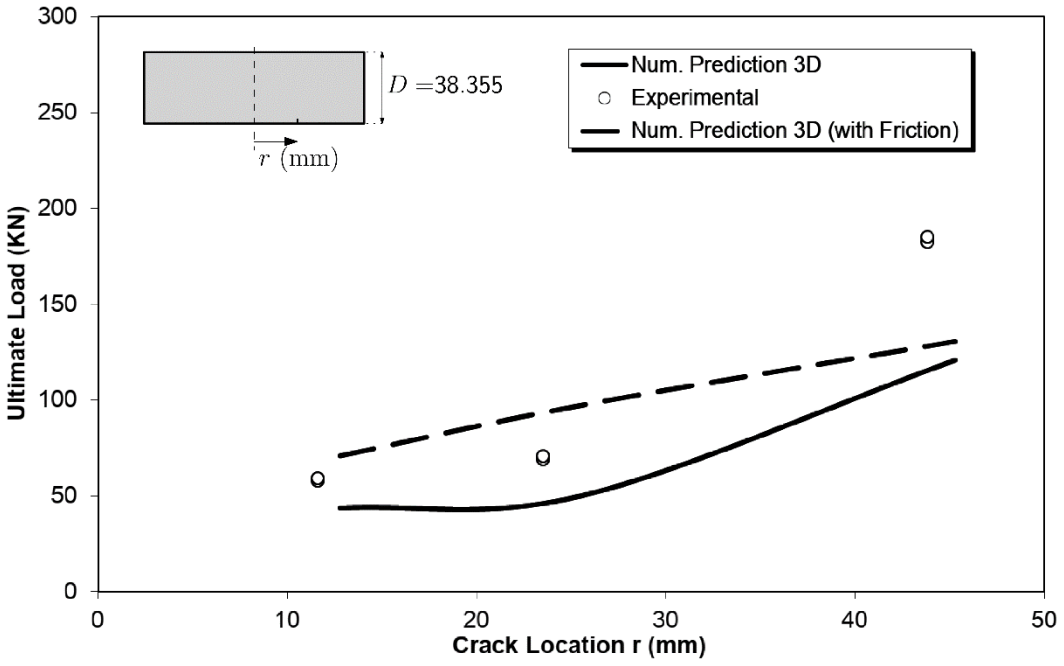

Figure 26: Effect of friction on breaking loads in circular plate specimens (*D*=38.3mm)

For circular plates, the breaking load curve including friction effects is above the experimental values for those cracks located at distances of *R*/2 and *R*/4 from the symmetry axis; however the curve is below the experimental breaking load for those cracks placed at the furthest location from the axis. The reason of this is that the stress intensity factor in mode I is negative due to the compressive stress field around the crack when the defect is close to the external support ring, therefore the fracture is driven by a combination of mode I and mode II.

The predicted breaking loads for those cracks were consequently derived assuming K_I to be zero in the fracture criterion. This approach is just a rough estimation because the 3D models used in the present work are not suitable to work with contact and friction effects between crack faces under a compressive stress field and therefore the predicted breaking loads should be carefully considered.

4. A damaged anchor head in an aggressive environment

This section presents an example that deals with a commercial anchor head with a small damage produced during machining, transport or placement. This damage is, in general, accepted because it fulfils all standards of geometry, chemical composition, non-corrosion, and nominal strength. This damage can be idealized, from the safe side, as a tiny crack (usually of tenths of a millimetre, difficult to detect during a routine control test) placed at the most critical zone.

A simplified anchor head geometry was selected with the purpose not to show up any commercial anchorage. A crack was placed in the transition region where tensile stresses reach maximum values. Stress intensity values for these cracks were previously obtained and are available in [17] and [29].

Table 6 summarises the mechanical properties of two materials used for manufacturing anchor heads, steel and cast iron. These properties were measured experimentally by means of standardised tests**.** Two values of the fracture toughness are given, since depending on the environmental conditions this parameter can be reduced, with a significant impact on the fracture behaviour of the element. The values of K_{ISCC} correspond to the stress-corrosion-cracking threshold behaviour in synthetic sea water, according to ASTM D1141-52 [30, 31]. In the case of steel, both values of K_{IC} are over 100 MPa·m$^{1/2}$, but in the case of cast iron, the value reduces from 60 to 35 MPa·m$^{1/2}$ under aggressive environmental conditions. Regarding the rest of the mechanical properties, both materials have acceptable strength and ductility according to usual design rules.

Table 6: Mechanical properties of steel and cast iron anchorages.

	E (GPa)	**$\sigma_{0.2}$ (MPa)**	**σ_{max} (MPa)**	**ε_m (%)**	**K_{IC} (MPa m$^{1/2}$)**	**K_{ISCC}* (MPa m$^{1/2}$)**
Steel	210	680	850	9	> 100	> 100
Cast iron	163	850	1100	5	60	35

ε_m = strain under maximum load

* Stress-corrosion-cracking threshold behaviour in synthetic sea water, according to ASTM D1141-52 [30]

Figure 27 shows the damage tolerance diagram for the considered anchor head. A steel anchorage, as the one reported in Table 6, will behave according to the line labelled with K_{IC} = 100 MPa m$^{1/2}$. A cast iron anchorage, with properties shown in Table 6, will perform according curves labelled 60 MPa m$^{1/2}$ or 35 MPa m$^{1/2}$, depending on the environmental conditions; in this case, the aggressive environment was sea water [31].

Under a design stress of 280 MPa, which is a standard value for the yield stress of a structural steel, the length of the critical crack that triggers brittle fracture is, according to Figure 27, about 25 mm for steel, 3.7 mm for cast iron under non-aggressive environment, or 0.54 mm in presence of sea water. As can be noticed, when the anchorage is not manufactured with the suitable material, a very small crack —generated during fabrication or grown by fatigue or corrosion— can become catastrophic.

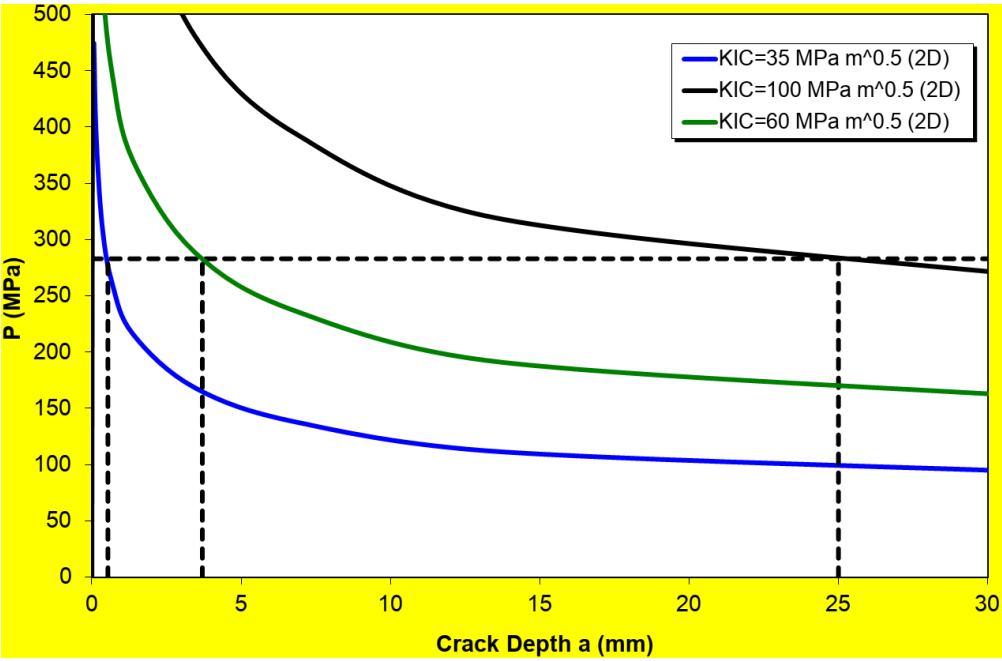

Figure 27: Design stress depending on anchorage material and environment.

5. Final comments and conclusions

This research has shown the role of defects on the loading capacity of structural components and how using the concept of damage tolerance can help in their structural design. The paper ends with an example, taken from actual anchor heads.

Breaking loads for circular transversally loaded discs and anchor heads have been evaluated using the concept of damage tolerance. Experimental results have shown the suitability of numerical procedures to predict ultimate loads, in general much lower than predicted by considering components without defects.

As a summary, two issues should be remarked; one related with design and another with material selection:

- Designing by using the concept of damage tolerance can be useful for optimizing the design of an element, although the defect characteristics can be difficult to define; in the case of the anchor head, analysed in this work, the relevance of the component depth and, particularly, of the transition angle θ, has been proved: smooth transitions provide higher breaking loads for the same defect, thus increasing the damage tolerance of the

element. This fact is illustrated in Fig. 13 where, for tiny cracks, the stress intensity factor is around two or three times smaller when the transition joint is circular with respect to more abrupt transitions, such as those with θ angle equal to 90º, 130º or 150º. This is related to a higher stress concentration in abrupt changes of thickness, which leads to a reduction of the breaking load, thus remarkably reducing the damage tolerance of the element.

- Finally, a needed property for damage tolerance design is the material toughness under the appropriate environment, a property not always available, since classical design —ignoring cracks— only needs Young modulus, yield stress, ultimate tensile strength and ductility. As the concept of damage tolerance becomes more usual, these data will be more accessible, meanwhile it is recommended to perform toughness tests with the material of choice [32, 33] and under the scheduled working environment.

These suggestions should help in designing safer structural components.

ACKNOWLEDGEMENTS

The authors gratefully acknowledge the financial support provided by the Ministry of Economy and Competitiveness of Spain by means of the Research Fund Project PID2019-108978RB-C31R.

References

[1] Chang, J. B., & Rudd, J. L. (Eds.). (1984). *Damage tolerance of metallic structures: Analysis methods and applications* (Vol. 842). ASTM International.

[2] Chowdhury, P., Sehitoglu, H., & Rateick, R. (2018). Damage tolerance of carbon-carbon composites in aerospace application. *Carbon*, 126, 382-393.

[3] Alderliesten, R. C. (2015). Designing for damage tolerance in aerospace: A hybrid material technology. *Materials & Design*, 66, 421-428.

[4] Tunes, M. A., Vishnyakov, V. M., & Donnelly, S. E. (2018). Synthesis and characterisation of high-entropy alloy thin films as candidates for coating nuclear fuel cladding alloys. *Thin Solid Films*, 649, 115-120.

[5] Tunes, M. A., & Vishnyakov, V. M. (2019). Microstructural origins of the high mechanical damage tolerance of NbTaMoW refractory high-entropy alloy thin films. *Materials & Design*, 170, 107692.

[6] Valiente, A., & Elices, M. (1998). Premature failure of prestressed steel bars. *Engineering Failure Analysis*, 5(3), 219-227.

[7] Samei, J., Pelligra, C., Amirmaleki, M., & Wilkinson, D. S. (2020). Microstructural design for damage tolerance in high strength steels. *Materials Letters*, 127664.

[8] Giannopoulos, I. K., Grafton, K., Guo, S., & Smith, H. (2020). Damage tolerance of CFRP airframe bolted joints in bearing, following bolt pull-through failure. *Composites Part B: Engineering*, 185, 107766.

[9] De Abreu, M., Iordachescu, M., & Valiente, A. (2014). Effects of hydrogen assisted stress corrosion on damage tolerance of a high-strength duplex stainless steel wire for prestressing concrete. *Construction and Building Materials*, 66, 38-44.

[10] Iordachescu, M., Pérez-Guerrero, M., Valiente, A., & Elices, M. (2018). Environmental effects on large diameter high-strength rods for structural applications. *Engineering Failure Analysis*, 83, 230-238.

[11] Shah, S. Z. H., Karuppanan, S., Megat-Yusoff, P. S. M., & Sajid, Z. (2019). Impact resistance and damage tolerance of fiber reinforced composites: A review. *Composite Structures*, 217, 100-121.

[12] Zerbst, U., Schödel, M., & Heyder, R. (2009). Damage tolerance investigations on rails. *Engineering Fracture Mechanics*, 76(17), 2637-2653.

[13] Zerbst, U., Schödel, M., & Beier, H. T. (2011). Parameters affecting the damage tolerance behaviour of railway axles. *Engineering Fracture Mechanics*, 78(5), 793-809.

[14] Zerbst, U., Beretta, S., Köhler, G., Lawton, A., Vormwald, M., Beier, H. T., & Klingbeil, D. (2013). Safe life and damage tolerance aspects of railway axles–A review. *Engineering Fracture Mechanics*, 98, 214-271.

[15] Wu, X., Chi, M., & Gao, H. (2016). Damage tolerances of a railway axle in the presence of wheel polygonalizations. Engineering Failure Analysis, 66, 44-59.

[16] Kolitsch, S., Gänser, H. P., & Pippan, R. (2017). Damage tolerance concepts for railway switch components. *Procedia Structural Integrity*, 4, 95-105.

[17] Gálvez, J. C., Elices, M., & Olivares, M. A. (2006). Damage tolerance of an anchor head in a post-tensioning anchorage system. *Engineering Failure Analysis*, 13(2), 235-246.

[18] Jiang, Q., Feng, X. T., Cui, J., & Li, S. J. (2015). Failure mechanism of unbonded prestressed thru-anchor cables: in situ investigation in large underground caverns. *Rock Mechanics and Rock Engineering*, 48(2), 873-878.

[19] Ganz, H. R. (2001). Evolution of prestressing systems. In Durability of Post-tensioning Tendons: Technical Report: Proceedings of a Workshop Held at Ghent University on 15-16 November 2001. fib Fédération internationale du béton. Vol. 15, p. 156.

[20] Anderson, T.L. (2004). *Fracture mechanics: fundamentals and applications*. CRC press.

[21] Guinea, G. V., Planas, J., & Elices, M. (2000). K_I evaluation by the displacement extrapolation technique. *Engineering fracture mechanics*, 66(3), 243-255.

[22] Marceau, D., Bastien, J., Fafard, M., & Chabert, A. (2001). Experimental and numerical studies of mono-strand anchorage. *Structural Engineering And Mechanics: An International Journal,* 12(2), 119-134.

[23] Marceau, D., Fafard, M., & Bastien, J. (2003). Constitutive law for wedge-tendon gripping interface in anchorage device-numerical modeling and parameters identification. *Structural Engineering And Mechanics: An International Journal*, 15(6), 609-628.

[24] ASTM International. (2015). ASTM D638-14, Standard Test Method for Tensile Properties of Plastics. ASTM International.

[25] ASTM International. (2014). D5045-14, Standard Test Methods for Plane-Strain Fracture Toughness and Strain Energy Release Rate of Plastic Materials" Annual Book of ASTM Standards, Part, 8.

[26] Gómez, F. J., & Elices, M. (2003). A fracture criterion for sharp V-notched samples. *International Journal of Fracture*, 123(3), 163-175.

[27] Gómez, F. J., & Elices, M. (2004). A fracture criterion for blunted V-notched samples. *International Journal of Fracture*, 127(3), 239-264.

[28] Polimetacrilato de metilo, (2011) https://tecnologiadelosplasticos.blogspot.com/2011/05/polimetacrilato-de-metilo.html (accessed 8 March 2021).

[29] Olivares, M. A. (2012). Estudio de la tolerancia al daño de los materiales y sistemas de pretensado (Doctoral dissertation, Universidad Politécnica de Madrid, *In Spanish*). 412 pages.

[30] ASTM International. (2021). ASTM D1141-98, Standard practice for the preparation of substitute ocean water. ASTM International.

[31] Caballero, L. Elices M. and Parkins, R.N. (2005), Environment sensitive fracture of austempered ductile iron, *Corrosion NACE*, 61 (1), pp. 51–57.

[32] ASTM International. (2021). ASTM E399-20, Standard Test Method for Linear-Elastic Plane-Strain Fracture Toughness of Metallic Materials. ASTM International.

[33] ASTM International. (2020). ASTM E1820-20, Standard Test Method for Measurement of Fracture Toughness. ASTM International.

Declaration of interests

☒ The authors declare that they have no known competing financial interests or personal relationships that could have appeared to influence the work reported in this paper.

☐ The authors declare the following financial interests/personal relationships which may be considered as potential competing interests: